RESEARCH ARTICLE

NANO · MICRO small
www.small-journal.com

Stabilizing Metal Halide Perovskite Films via Chemical Vapor Deposition and Cryogenic Electron Beam Patterning

Randy Burns, Dylan Chiaro, Harrison Davison, Christopher J. Arendse, Gavin M. King, and Suchismita Guha**

Halide perovskites are hailed as semiconductors of the 21st century. Chemical vapor deposition (CVD), a solvent-free method, allows versatility in the growth of thin films of 3- and 2D organic–inorganic halide perovskites. Using CVD grown methylammonium lead iodide ($MAPbI_3$) films as a prototype, the impact of electron beam dosage under cryogenic conditions is evaluated. With 5 kV accelerating voltage, the dosage is varied between 50 and 50000 μC cm^{-2}. An optimum dosage of 35 000 μC cm^{-2} results in a significant blue shift and enhancement of the photoluminescence peak. Concomitantly, a strong increase in the photocurrent is observed. A similar electron beam treatment on chlorine incorporated $MAPbI_3$, where chlorine is known to passivate defects, shows a blue shift in the photoluminescence without improving the photocurrent properties. Low electron beam dosage under cryogenic conditions is found to damage CVD grown 2D phenylethlyammoinum lead iodide films. Monte Carlo simulations reveal differences in electron beam interaction with 3- and 2D halide perovskite films.

1. Introduction

The steep performance improvement in organic–inorganic halide perovskite solar cells[1] over the past decade has resulted in exploiting their optical and electronic properties in a vast range of optoelectronic devices such as light-emitting diodes, lasers, photodetectors, transistors, spintronic, and memory devices.[2–6] The 3D systems with monovalent cations (A), bivalent metal cations (M), and halide anions (X) share the general formula of AMX_3. The A cations such as methylammonium (MA) or formamidinium (FA) occupy cages formed by the corner sharing the inorganic octahedra (MX_6). Pb or Sn are the most common choices for the M cation. The optical properties in these materials emerge from excitonic physics, which is further enhanced in 2D organic-inorganic halide perovskites (OIHP)[7] where a layer of the MX_6 octahedra is interspersed with a barrier layer comprising long organic cations, forming a type-I quantum-well architecture since the electron-hole pairs are confined to the perovskite layer.

Stressors such as moisture, local heating, and illumination by ultraviolet light decompose the OIHP into its precursor elements. The degradation of $MAPbI_3$ upon exposure to moisture occurs at the hydrogen bond between the MA^+ cation and the $[PbI_6]^{4-}$ inorganic units.[8] Although a nominal concentration of moisture is known to promote crystallization during the growth of $MAPbI_3$,[9] exposure to excess moisture results in its decomposition into its precursors and hydrated phases. A combination of 3D and 2D perovskites is, however, seen to prevent moisture degradation.[10] Furthermore, the long-term stability of $MAPbI_3$ solar cells even in a N_2 atmosphere could be challenging if temperatures are in the normal operating range of ≈85 °C.[11] Towards enhancing the air stability of OIHPs, several strategies including the use of antisolvents have been used for solution processed thin films.[12,13] Chemical vapor deposition (CVD), without the use of any solvents, has resulted in more air stable films compared with spin-coated films. Without any encapsulation and with storage under ambient conditions, solar cells using CVD grown $MAPbI_3$ films were found to be stable for up to three weeks.[14] However, residual PbI_2 is often an issue with both spin-coated and CVD grown films. Although slight excesses of PbI_2 can passivate defects, too much may be detrimental

R. Burns, D. Chiaro, H. Davison
Department of Physics and Astronomy
University of Missouri
Columbia, MO 65211, USA

C. J. Arendse
Department of Physics and Astronomy
Nano-Micro Manufacturing Facility
University of the Western Cape
Bellville 7535, South Africa

G. M. King
Department of Physics and Astronomy
Department of Biochemistry
and MU Materials Science and Engineering Institute
University of Missouri
Columbia, MO 65211, USA
E-mail: kinggm@missouri.edu

S. Guha
Department of Physics and Astronomy and MU Materials Science and Engineering Institute
University of Missouri
Columbia, MO 65211, USA
E-mail: guhas@missouri.edu

The ORCID identification number(s) for the author(s) of this article can be found under https://doi.org/10.1002/smll.202406815

DOI: 10.1002/smll.202406815

to device performance where large hysteresis in current-voltage sweeps is seen. Chlorine complexes in iodide perovskites are known to passivate defects. Chlorine in the precursor solution-processed films (PbICl or $PbCl_2$) was seen to stabilize the final perovskite film $MAPbI_3$.[15] Doping with $RbCl_2$ forms an inactive PbI_2-$RbCl_2$ complex that is effective in stabilizing the perovskite phase.[16] Using a three-step CVD process, our earlier work has shown that the formation of an intermediate PbICl complex resulted in $MAPbI_3$ films with the same structural phase over a temperature range from 20 to 300 K.[17]

Understanding the degradation pathways in halide perovskites at the atomic scale has been challenging since these materials are electron-beam (e-beam) sensitive.[18] Although transmission electron microscopy (TEM) has been used for mapping the overall morphology of OIHPs,[19] mapping at the atomic scale has been an insurmountable task. Cryo-electron microscopy (EM) techniques, however, are promising and have demonstrated the degradation pathway at the nanoscale in $MAPbI_3$ due to moisture,[20] and other defects.[21] Furthermore, patterning OIHPs for nanoscale devices has remained a challenge due to both e-beam damage as well as limitations of an appropriate resist material. The success of cryo-EM suggests that cryogenic conditions may allow a viable route towards nanopatterning OIHPs with an e-beam. The work by Jin and co-workers have demonstrated the feasibility of e-beam treatment on OIHPs under cryogenic conditions.[22,23] However, these studies were conducted on solution-processed spin-coated samples. CVD provides an alternate route for the growth of OIHP films with a high degree of controllability and thus far, e-beam patterning techniques have not been demonstrated on such films.

CVD and other physical vapor deposition techniques have been adopted by several research groups for the synthesis of OIHP films[24–27] including 2D OIHPs.[28,29] A two-step low pressure CVD method developed in our prior work was seen to produce high quality $MAPbI_3$ films. The first step involves the formation of a PbI_2 film in a CVD reactor which is then converted by MAI vapors to form the perovskite film.[14,30] The increased air stability of these CVD grown films is believed to be due to a combination of excellent surface coverage with reduced moisture-trapping pinholes and well-oriented vertical columnar grains. $MAPbI_3$ undergoes structural phase transitions as a function of temperature. Under ambient conditions, $MAPbI_3$ is typically in the tetragonal phase (space group (SG) *I4/mcm*) and undergoes a phase transition at 320 K to a cubic phase (SG: $pm\bar{3}m$). Further, a tetragonal to an orthorhombic (SG: *Pnma*) phase transition occurs below 160 K.[31–33] However, it should be noted that since the three phases are so closely related to the octahedral tilt of the PbI_6 cage and orientational ordering of the MA^+ ions, the phase transition temperatures are strongly dependent on the growth method and annealing conditions.[25,34] Using a three step CVD process starting with lead chloride to form the perovskite film: $PbCl_2 \rightarrow PbICl \rightarrow MAPbI_3$, we found the sample to remain in the same phase (SG: *I4/mcm*) throughout the temperature range from 20 to 300 K.[17] It should be pointed out that Cl mainly acts as a dopant or a passivating agent since no trace of Cl could be found after conversion into the perovskite film ($MAPbI_3$). These two perovskite films: two-step CVD grown $MAPbI_3$ and three-step CVD grown $MAPbI_3$:Cl initiated by $PbCl_2$ have identical optical properties under ambient conditions and thus form a test-bed for comparison of e-beam treatment and patterning to evaluate their stability and optical properties. The synthesis steps for these two perovskites are shown in **Figure** 1a,b. A scanning electron microscope image of the $MAPbI_3$ film, synthesized using a two-step process, depicts the average grain size to be larger than 1 µm. We note that the grain size of $MAPbI_3$:Cl is smaller (≈500 nm) compared with $MAPbI_3$.[17] Further, prior work has demonstrated the success of a two-step CVD process for the growth of high quality 2D OIHPs based on phenylethylammonium and butylammonium cations.[29]

Ice lithography, a nanopatterning technique using ice resists such as frozen water or organic solvents, offers a path for patterning delicate, free-standing, or 3D structures.[35–37] Although this technique was demonstrated almost two decades ago,[38] commercial unavailability of a scanning electron microscope (SEM) with a cryogenic stage combined with a metal deposition chamber has been a bottleneck towards making it a mainstream nanopatterning tool. A recent demonstration of patterning metal contacts on $MAPbBr_3$ nanoplates using water and other ice resists is an encouraging direction toward achieving perovskite nanoelectronics.[23]

As a first step towards patterning CVD grown OIHPs with an e-beam, in this work we use cryogenic conditions with the samples at 110 K for irradiating the films. The photoluminescence (PL) from $MAPbI_3$ and $MAPbI_3$:Cl blue shifts along with a strong enhancement in intensity when exposed to the e-beam. For photocurrent measurements, the e-beam patterning was achieved in a small channel region of 20 or 40 µm × 1000 µm. A strong enhancement in the photocurrent upon irradiating with a wavelength of 532 nm is observed in e-beam patterned $MAPbI_3$, which is, however, not observed in e-beam patterned $MAPbI_3$:Cl. Our results show that low e-beam dose under cryogenic conditions contributes to enhanced stability and optical properties in $MAPbI_3$, resulting in an improved photocurrent which most likely arises due to the purging of defect sites. In $MAPbI_3$:Cl, where Cl is already known to passivate defect sites, the e-beam irradiation has almost no effect in improving the photocurrent properties. E-beam patterning of 2D OIHPs was also carried out; however, in this case the films were severely damaged even with a very low dose of the e-beam. Monte Carlo simulations provide insights into the differences between e-beam interaction in 3D and 2D OIHPs.

2. Results and Discussion

The two-step CVD growth of $MAPbI_3$ mainly results in films that are in the tetragonal phase at room temperature. Detailed temperature-dependent synchrotron-based x-ray diffraction (XRD) studies from $MAPbI_3$ films, shown in **Figure** 2a, highlight the typical structural phases as reported in literature with the orthorhombic (*Pnma)* phase appearing below 150 K. Representative Le Bail fits at 300 and 120 K are shown in Figure 2b. Figure 2c plots the PL data as a function of temperature. It should be noted that only one PL peak at 770 nm is seen throughout the temperature range of 20-300 K. This is contrary to several solution processed $MAPbI_3$ samples reported in literature where the tetragonal ↔ orthorhombic phase transition is marked by two PL peaks.[22,39] Our results, therefore, suggests that temperature-dependent PL data is not always in lockstep with phase

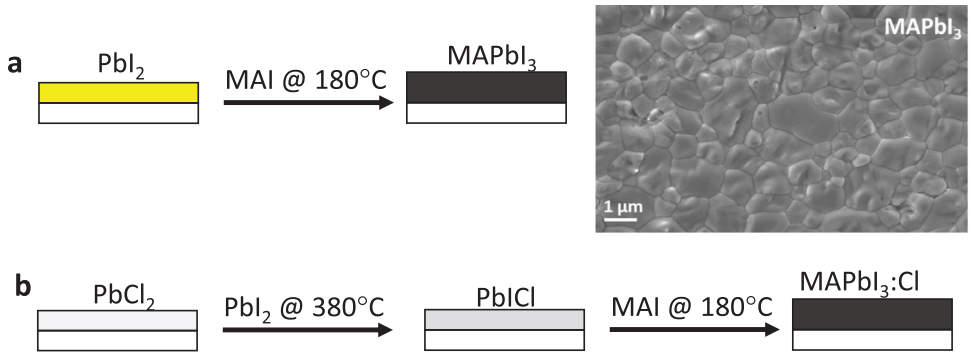

Figure 1. CVD synthesis steps. a,b) Two- and three-step synthesis of $MAPbI_3$ and $MAPbI_3$:Cl films, respectively. c) SEM image of $MAPbI_3$, which was synthesized by a two-step process without the addition of any chlorine.

transitions in OIHPs; the two peak PL is more likely a hallmark of defect emission and the excitonic recombination.[29] As reported earlier, detailed temperature-dependent XRD measurements from $MAPbI_3$:Cl conclusively showed that the sample remains in the tetragonal phase throughout a broad temperature range (20–300 K).[17]

2.1. E-Beam Grid Patterning: Photoluminescence Properties

The OIHP films were grown on SiO_2/Si^{++} substrates. A square grid with 2 µm × 2 µm e-beam irradiated square tiles with 2 µm spacing and overall dimensions of 32 µm x 32 µm was produced through irradiation from an electron beam with an acceleration voltage of 5 kV while the sample was under vacuum at 110 K. **Figure 3** shows the PL position and intensity from the e-beam treated area of the $MAPbI_3$ film. The dosage of each tile was varied according to Dose $= 50 + 794m + 6343n$ µC cm^{-2}, where m and n are indices which correspond to the row and column number respectively wherein $m, n = 0, 0$ corresponds to the tile in the top left corner as demonstrated in Figure 3a. The highest dose was 50 000 µC cm^{-2}, which corresponds to the bottom rightmost tile. The PL from the e-beam treated area was measured by a high-resolution spectrometer using a confocal microscope (with spectral resolution of 0.01 nm), where each individual tile was exposed to a 514 nm laser excitation. The PL intensity map (in blue and red color) as a function of the e-beam dosage is superimposed on the optical image of the sample in Figure 3b. With an increase in e-beam dosage, there is a significant increase in the measured PL intensity with the highest dosage of 50 000 µC cm^{-2} tile experiencing a fivefold increase in intensity. Figure 3d plots the PL spectrum from an untreated area, where the central peak is at 770 nm. Figure 3c is a raster scan of the PL spectra across the patterned squares from the top left to the bottom right of Figure 3b. Along with increasing PL intensity as a function of the e-beam dosage, a blueshift of the PL energy compared with the PL from the untreated area is observed, similar to the work by Jin et al.[22] As the beam dosage was increased from 50 to 50000 µC cm^{-2} in grid patterning, there was, however, no further blue shift of the PL.

It should be noted that the optical illumination spot size of 3 µm for the e-beam treated area is of the same order as the grain size (Figure 1c) and combined with high spectral resolution, interference effects are observed in the PL (Figure 3c). Interference

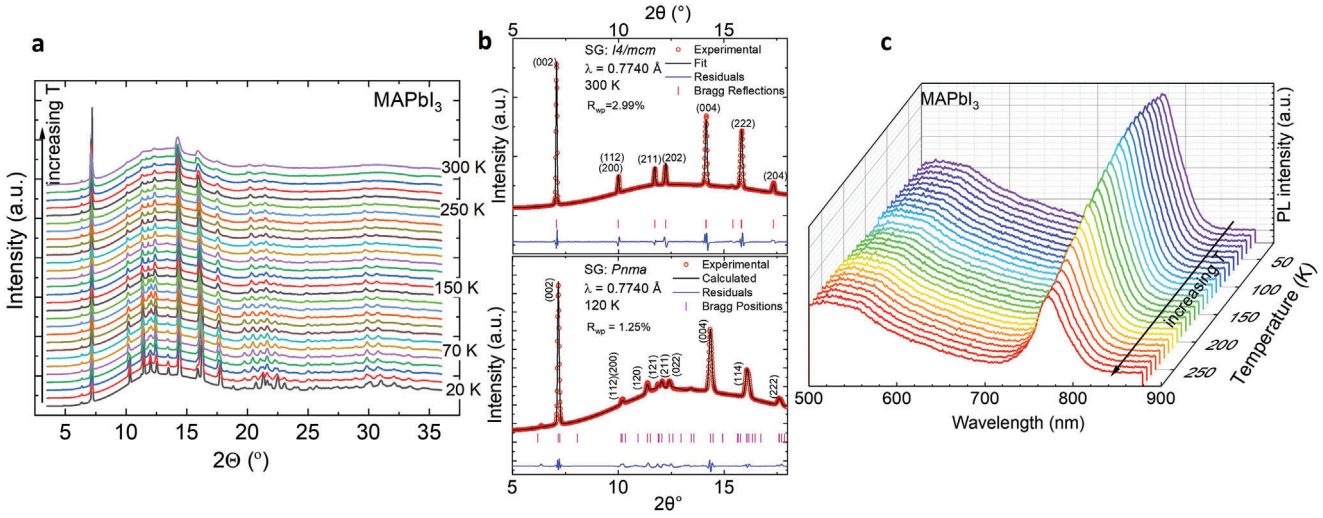

Figure 2. Temperature-dependent XRD and PL from CVD grown $MAPbI_3$. a) XRD pattern from 20 to 300 K at intervals of 10 K. b) Le Bail fits at 300 and 120 K. The red circles are the experimental data. The black line represents the fit. c) PL spectra from 20 to 300 K.

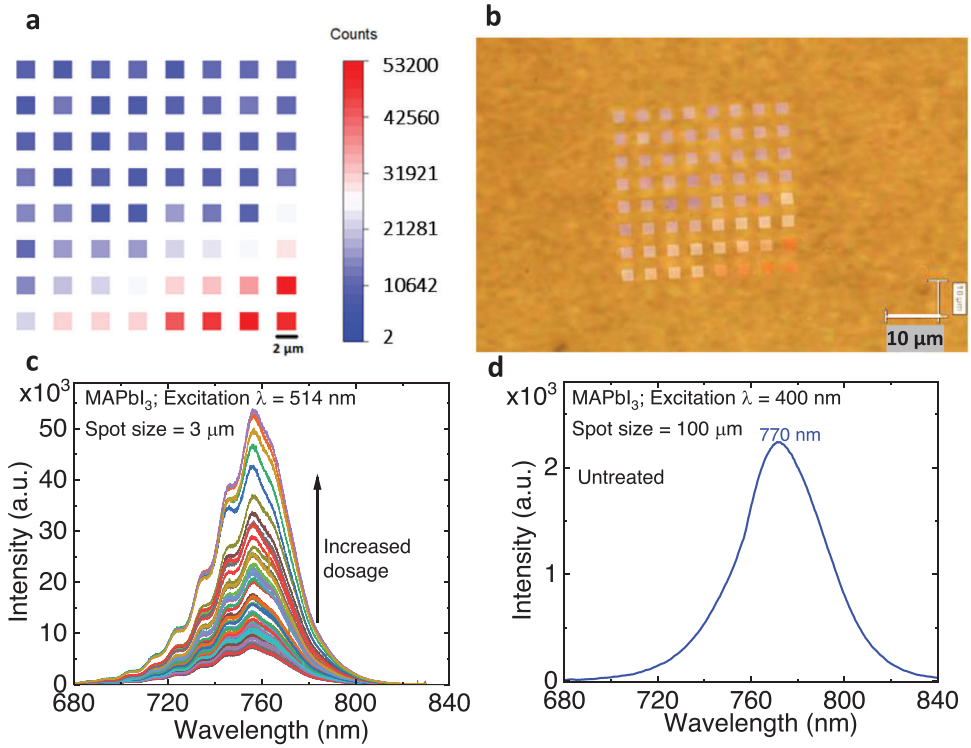

Figure 3. PL properties from an e-beam patterned grid in $MAPbI_3$. a) PL intensity of each individual e-beam irradiated tile. Tile (7,7) exhibits the strongest PL response, over five times higher than the top left. b) Optical image of the irradiated tiles superimposed with the PL intensity of each. c) PL spectrum of each individual tile as a function of increased dosage from 50 to 50000 µC cm^{-2}. d) PL spectrum of a reference untreated $MAPbI_3$ thin film, measured with a low-resolution spectrometer.

effects in PL have been observed in other photovoltaics thin film materials such as $Cu(In,Ga)Se_2$ (CIGS).[40,41] These effects are more pronounced in a back-reflection geometry where the surface normal to the sample is at 0° to the detector. Comparing Figure 3c,d, we note that the PL from an untreated area of the sample was measured with a low-resolution spectrometer (spectral resolution of 0.5 nm) with a geometry that was not in perfect back-reflection.

In the study by Jin et al.,[22] where spin-coated OIHP films were used, the maximum dose received by any individual tile of $MAPbI_3$ was 24800 µC cm^{-2} by which point the PL response significantly decreases; a dose of 13300 µC cm^{-2} showed the maximum PL intensity. Evidently, our CVD deposited OIHP films show increased resilience towards e-beam induced stimuli as compared to the spin-coated films. SEM images of the untreated and treated areas of $MAPbI_3$, close to the highest dose, are shown in Supporting Information. The morphology of the e-beam treated and untreated films looks similar, although there is an apparent etching of the top layer as discussed in Section 2.3.

A similar e-beam treatment was also performed for CVD grown $MAPbI_3$:Cl films. Since for this sample the structural phase remains throughout in the tetragonal phase,[17] e-beam irradiation at 110 K implies that unlike for the $MAPbI_3$ sample which undergoes a phase transition to the orthorhombic phase during irradiation, the Cl incorporated sample remains in the tetragonal phase. As observed in ref. [17] the perovskite grain sizes in $MAPbI_3$:Cl are smaller than in $MAPbI_3$, which arises due to the inherent small grain sizes of the intermediate mixed halide of PbICl. Once the sample was cooled to approximately 110 K, a resistive heater was used to increase the temperature with images taken at a variety of temperatures (Figure S3, Supporting Information). Also, the morphology of the film is unchanged after e-beam patterning (Figures S4 and S5, Supporting Information). This sample also shows an enhancement in the PL intensity along with a blue shift (see Supporting Information). The high defect density at grain boundaries is the origin for e-beam induced morphology changes.[42] Therefore, the lack of morphology changes, particularly at the grain boundaries, confirms the structural integrity of the CVD grown films. Unlike mixed-halide perovskites, where photo-induced phase segregation may occur due to the migration of iodine (I) ions towards the grain boundaries,[43,44] the three-step CVD growth results in perovskite films where no trace of Cl is detected at least by energy dispersive X-ray spectroscopy or X-ray photoelectron spectroscopy.[17,45] Cl acts more like a dopant during the growth process, passivating the defects. It is unlikely that after e-beam treatment, there would be any Cl migration. However, to obtain full insights into any phase segregation and passivation at the grain boundaries, Kelvin probe force microscopy[46] and shear-force scanning probe microscopy[47] investigations may be required. Such studies reveal how the electronic bands bend at the grain boundaries and the nature of the driving force behind I-phase separation.

The e-beam interacts with the sample mainly by purging the top surface layer of the perovskite which can contain a variety of defects. It is reported that, for a pristine and defect-free $MAPbI_3$

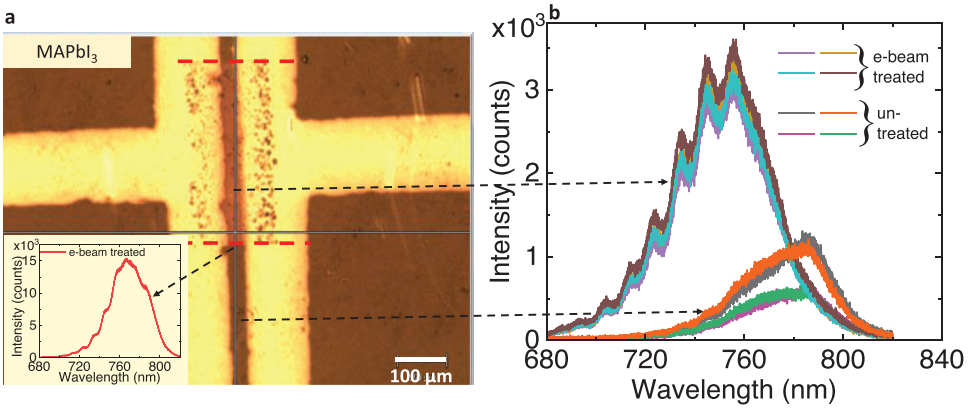

Figure 4. a) Optical image of the surface of $MAPbI_3$ with gold contacts thermally evaporated on top with a treated channel region. The inset shows the PL at the bottom boundary between the treated channel and untreated channel region, marked by the red dashed lines. This PL has the highest intensity of any region several times over in addition to an intermediate blue shift between the untreated and fully treated regions. b) PL spectra of the interior treated channel and the untreated channel regions. Points within channel show large blue shifts to ≈750 nm in addition to a threefold increase in PL intensity.

sample, the activation energy required to dislodge an I atom from the ionic bond with Pb is ≈4.05 eV whereas samples that contain point defects such as halogen vacancies have a lower activation energy of ≈3.5 eV.[48] As a consequence, surfaces with more defects exhibit an increased vulnerability towards the e-beam irradiation process. We posit that the resulting surfaces are more likely to contain fewer defects that would lower the activation energy of any process which results in dissociation of ionic bonds. As the higher defect density surface is effectively removed from the sample, the remaining material then displays enhancement in PL and other characteristics. One should expect for thin films with an intrinsically lower defect density that higher dosages of the e-beam are required to observe the same effects in samples with more defects. This could explain the higher dose requirements of the CVD grown $MAPbI_3$ thin films compared to the spin- coated samples in order to see a similar increase in the PL intensity and a blue shift of the PL spectrum.

2.2. E-Beam Continuous Patterning: Photoluminescence and Photocurrent

As a next step of cryogenic e-beam patterning, a continuous region in a narrow channel region demarcated by gold electrodes on OIHP films was carried out. After the CVD growth of the perovskite films on SiO_2/Si^{++} substrates, gold contacts with a narrow channel region of 25 and 50 µm were evaporated on the films. These architectures served as three-terminal devices for dynamic photocurrent measurements. In addition to measuring the photocurrent, the advantage of this patterning style is that it allows us to capture the PL from a region where the sample is e-beam treated versus a region in the same channel, where it was not treated. The channel region was exposed to a uniform e-beam dosage of 35 000 µC cm^{-2}.

An optical image from $MAPbI_3$ in **Figure 4a** highlights the e-beam treated area between the two dashed red lines. The discoloration of the film compared to the surrounding areas clearly demonstrates the optical effects of the treatment. In order to confirm that the discolored region corresponded to an enhanced, treated $MAPbI_3$ instead of an undesired de-converted PbI_2 region, PL measurements were carried out within, above and beneath the channel. Figure 4b demonstrates a greatly enhanced PL intensity for every spot measured within the e-beam treated area that is roughly three times more intense compared to the PL intensity from regions that were not treated by the e-beam. Additionally, we now observe a clear blue shift of the PL peak from ≈775 to ≈750 nm that was less pronounced in the grid exposure in the previous section. Similar changes in the PL are observed in the $MAPbI_3$:Cl sample after e-beam treatment (see Figure S7, Supporting Information).

Although, in the case of the grid, the highest dose received was 50 000 µC cm^{-2}, the completely contiguous treatment of the channel appears to have received a higher effective dose than the individual grid tiles. It should be noted that the overall e-beam exposure time plays a role, which is longer in the contiguous treatment compared with the individual 2 µm × 2 µm grid. With this dose of 35 000 µC cm^{-2}, the blue shift of the PL energy is realized in addition to an enhancement in intensity. The PL was also measured at the very thin boundary region at the edge of the channel as shown in the inset of Figure 4a. At this location, the blue shift in PL appears to be in an intermediate wavelength of ≈765 nm between the fully treated channel and the untreated surrounding areas. Additionally, this boundary region which received an intermediate dose has a greatly enhanced PL that is ≈15 times the intensity of the untreated region and even ≈3 times the intensity of the channel. This implies that the optimal PL intensity response occurs at a dosage less than is required to observe the maximal blue shift and that it does not directly correlate with a minimal amount of defect states.

2.2.1. Photocurrent Measurements

The photocurrent was measured by exciting a 532 nm line from a laser diode as a function of the incident power in the channel region of two independent devices, one where part of the

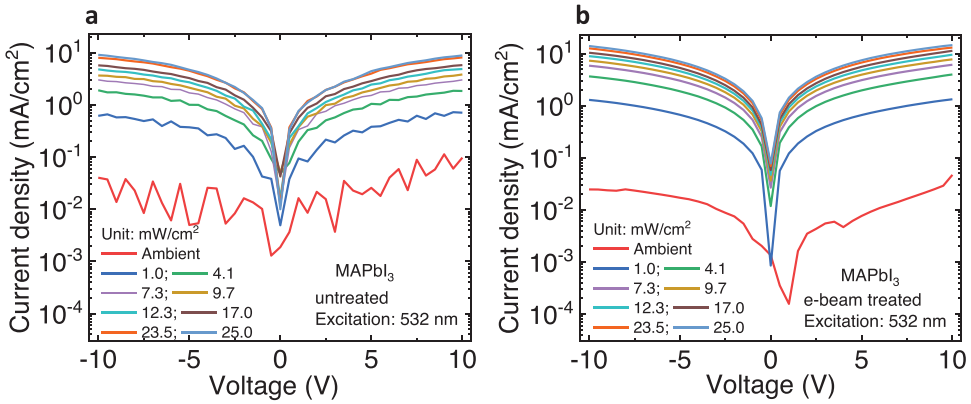

Figure 5. a) Photocurrent of $MAPbI_3$ for an untreated channel. b) Photocurrent of $MAPbI_3$ for a treated channel. The treated channel has a photocurrent magnitude that is greater by a factor of ≈5. The lateral voltage across the contacts is plotted on the horizontal axis.

channel region was exposed to the e-beam as shown in Figure 4a and another where there was no e-beam treatment. **Figure** 5a,b compares the photocurrent of two such $MAPbI_3$ devices with a voltage sweep from −10 to +10 V across the two contacts. The e-beam irradiation treatment of the sample consistently resulted in an increase in the photocurrent magnitude of roughly a factor of 5 as seen in the semi-log current density versus voltage plots. The increase in the photocurrent magnitude is attributed to a reduction of defects states in the top layer of the perovskite film after exposure to the e-beam. Surprisingly, the $MAPbI_3$:Cl samples show no changes in the photocurrent upon e-beam treatment. For a better comparison of the photocurrent between $MAPbI_3$ and $MAPbI_3$:Cl and understanding the nature of the photocarriers including under e-beam irradiation treatment, dynamic photocurrent measurements were carried out.

The dynamic photocurrent measurements were conducted under a fixed laser (λ = 532 nm) power density of 10 mW cm^{-2} with a chopper frequency of 2 Hz. **Figure** 6a–d plots the transient photocurrent response from four devices: untreated and e-beam treated $MAPbI_3$ and $MAPbI_3$:Cl. Due to the three-terminal

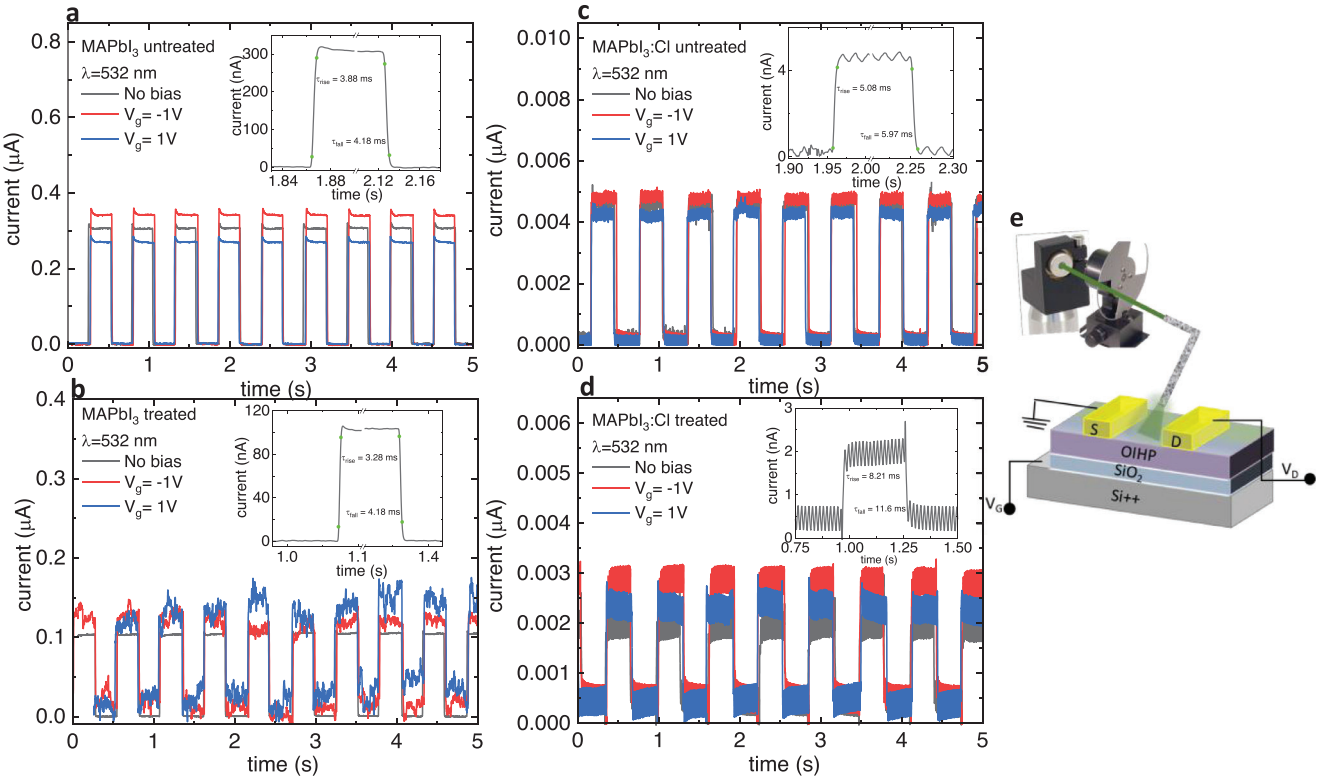

Figure 6. Dynamic photoresponse measurements. Current versus time under 532 nm illumination under no bias (black line), −1 V (red line), and +1 V (blue line) biases for a) untreated $MAPbI_3$, b) e-beam treated $MAPbI_3$, c) untreated $MAPbI_3$:Cl, and d) e-beam treated $MAPbI_3$:Cl. The insets show the response times with the green dots depicting 10% and 90% of the photocurrent during the rise and fall cycles. e) Schematic of the device and the setup.

Table 1. Photoresponse rise and fall times.

Sample	τ_{rise} [ms]	τ_{fall} [ms]
Untreated $MAPbI_3$	3.88 ± 0.30	4.18 ± 0.30
e-beam treated $MAPbI_3$	3.28 ± 0.30	4.18 ± 0.30
Untreated $MAPbI_3$:Cl	5.08 ± 0.30	5.97 ± 0.30
e-beam treated $MAPbI_3$:Cl	8.21± 0.20	11.60 ± 0.20

device architecture, as schematically shown in Figure 6e, the gate bias (V_g) could be independently varied as the photocurrent was measured by applying a voltage of −10 V between the source (S) and the drain (D) terminals. The absolute photocurrent between each pair of samples is non-commensurate since there was some shadowing effect of the gold electrodes and, although the $MAPbI_3$ e-beam treated and untreated device measurements were from 25 µm channel lengths, there was a 20% decrease in the channel length in the untreated sample which increased the overall magnitude of the photocurrent. Similarly, for the $MAPbI_3$:Cl samples, the untreated device represents a 25 µm channel length whereas the e-beam treated device represents a channel length of 50 µm. However, the overall trends and the response times from the individual devices can still be compared.

The untreated $MAPbI_3$ device (Figure 6a) shows a clear enhancement in the photocurrent with a gate bias of $V_g = -1$ V and a decrease in the photocurrent with a gate bias of $V_g = 1$ V compared with the no bias condition. This trend is also seen in the untreated $MAPbI_3$:Cl device (Figure 6c), albeit not as clearly as in $MAPbI_3$. It should be noted that the devices do not perform as transistors, i.e., under these low bias voltages, there is no additional charge injection, and the current primarily arises due to the photocarriers which are generated by the incident light. The e-beam treated $MAPbI_3$ device, on the other hand (Figure 6b), does not show a distinction in the photocurrent when V_g is switched from +1 to −1 V, and additionally, the dynamic photocurrent becomes noisy with the application of the bias. The e-beam treated $MAPbI_3$:Cl device (Figure 6d) shows a similar trend of the photocurrent upon switching the bias from +1 to −1 V as its untreated counterpart (Figure 6c). The insets show the response of the photocurrent in terms of the rise (τ_{rise}) and decay (τ_{fall}) times, where τ_{rise} is defined as the time it takes for the photocurrent to increase from 10% to 90% of its maximum value and τ_{fall} is the time for the maximum photocurrent to decrease from 90% to 10% of its value. The response times were obtained from the unbiased devices and are tabulated in **Table 1**.

OIHPs are known for their dual nature of conduction with mixed ionic-electronic transport.[49–52] Not only do ions enhance the conductivity in perovskite solar cells but they also modify the internal electric field due to the accumulation of ions at interfaces.[53] Transient capacitance measurements from vertical architectures have revealed the presence of multiple ionic species.[54] Our observation for the untreated $MAPbI_3$ device suggests that the increase/decrease in the photocurrent upon switching the bias arises from trapping of ions at defect sites. Negative V_g implies trapping of positive ions such as MA^+ which may alter the internal electric field in a way that the overall photocurrent is enhanced. A positive bias which may trap the negative ions (I^-) has a reverse effect on the overall photocurrent. As the above PL studies suggest that the e-beam treatment passivates defect sites in $MAPbI_3$, it could mean less favorable trapping sites for ions in a three-terminal architecture without providing a pathway for altering the internal field. The response times (for the unbiased condition), however, are comparable with the untreated $MAPbI_3$ device. The rise time is faster for the e-beam treated device. It should be noted that the overall photocurrent is much higher for the e-beam treated $MAPbI_3$ device (Figure 5); interface biasing simply provides a tool for further validation that the defect sites in $MAPbI_3$ are passivated upon e-beam treatment. The situation in $MAPbI_3$:Cl is quite different. Since Cl has been known to already passivate defects, the e-beam treatment does not further improve the photocurrent properties. If anything, the response times increase for the e-beam treated device.

Overall, e-beam irradiation of 3D OIHP films under cryogenic conditions is seen to impact the PL and photocurrent properties, and our results suggest there may be at least two different effects. The blue shift of the PL energies in $MAPbI_3$ has been typically associated with structural changes. Under pressure, for example, $MAPbI_3$ undergoes a structural phase transformation from the tetragonal (SG: *I4/mcm*) phase to a cubic phase II (SG: $Im\bar{3}$) at ≈0.4 GPa[55] and at a slightly lower pressure of 0.25 GPa in CVD grown $MAPbI_3$.[30] This phase transition is associated with a blue shift of the PL energy due to an enhanced octahedral tilting.[55] After e-beam irradiation, both $MAPbI_3$ and $MAPbI_3$:Cl samples show a blue shift along with an intensity enhancement of the PL. This change in the PL may be related to a structural change, similar to what is seen under high pressure. Future x-ray diffraction studies from the e-beam exposed part of the sample will be beneficial for obtaining a complete understanding of the structural changes. The photocurrent studies, on the other hand, point in the direction of a reduction of defect states in the $MAPbI_3$ film after exposure to the e-beam. In $MAPbI_3$:Cl, where the PbICl phase helps with the stability of the final perovskite film due to an effective stress release along with a passivation of defects due to residual $PbCl_2$,[15] the e-beam irradiation does not further contribute to the passivation of defect sites.

2.3. E-Beam Propagation Simulations

E-beam irradiation typically results in three modes of damage: displacement, ionization or radiolysis, and electrostatic charging.[18] Under cryogenic conditions, these damage routes are mitigated in $MAPbI_3$ as seen in this work. However, when we irradiated the 2D organic-inorganic halide perovskite, phenylethylammonium lead iodide (PEA_2PbI_4), grown by CVD, with a much a lower dose of the e-beam compared with the 3D system, there was severe damage to the film (Figure S8, Supporting Information). The damage in 2D perovskites is most likely due to radiolysis, which is material dependent. In order to understand these differences between the 3D and 2D perovskite samples, we modeled the effects of e-beam irradiation on perovskite thin films using a Monte Carlo program, CASINO (V3.3),[56] which is designed to calculate electron-sample interactions in SEM.[57] The program allows for the implementation of a variety of physical models and can simulate 3D sample geometries. We implemented the model by Browning et al.[58] for electron cross section and the model by Joy and Luo[59] for energy loss. These

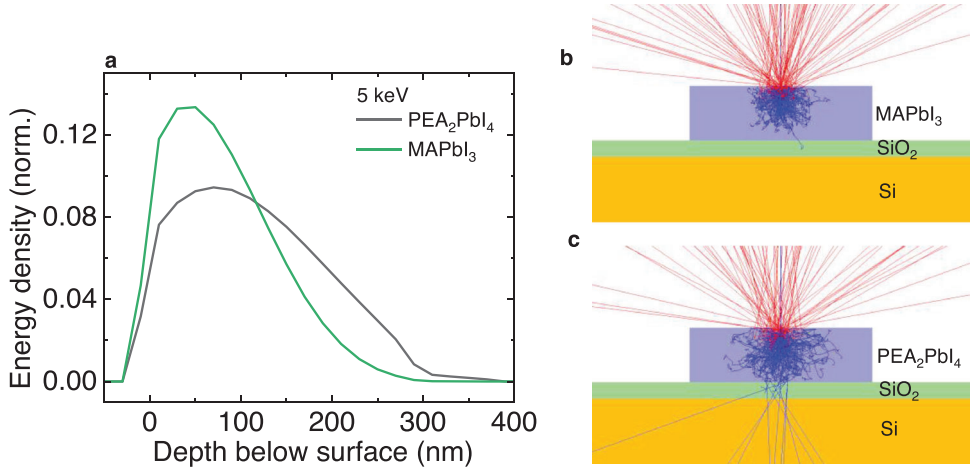

Figure 7. a) Simulation of normalized energy density distribution in PEA_2PbI_4 and $MAPbI_3$ by 5 keV e-beam. Representation of 200 arbitrarily selected electron trajectories in b) $MAPbI_3$ and c) PEA_2PbI_4 slabs of 1 μm × 1 μm and 300 nm thickness. The e-beam trajectory was simulated with the perovskite layers being placed on 90 nm SiO_2 and infinitely thick Si to match the experimental conditions. The blue lines represent the primary beam, and the red lines represent backscattered electrons.

models assume gradual medium-dependent energy loss along a trajectory punctuated by elastic scattering events. The program generates an energy scan, representing the energy density deposited by the incident beam throughout the sample. We integrated these values over the XY plane (normal to the beam) to determine energy deposition as a function of depth.

Figure 7 shows the results of our simulations. 10^6 electron trajectories at 5 keV were simulated in $MAPbI_3$ and PEA_2PbI_4 with mass densities of 4 and 2.55 g cm^{-3}, respectively. The perovskite slabs of 1000 nm × 1000 nm by 300 nm thickness were modeled on a 90 nm SiO_2 layer placed on an infinitely thick Si layer to match the experimental condition. Figure 7a demonstrates the normalized energy distribution of incident electrons along with a visual representation of backscattered (red lines) versus primary beam electrons (blue lines) in Figure 7b. The mean penetration depth into $MAPbI_3$ was 79.9 nm and into PEA_2PbI_4 was 110.9 nm. Implementation of other physical models yielded similar results. The significantly higher mass density of $MAPbI_3$, as compared to the 2D perovskite PEA_2PbI_4 containing light, organic spacer regions facilitate a faster attenuation of the electrons along the depth of the sample. Consequently, the incident electrons distribute energy more densely amongst the top layers of the 3D perovskite and travel deeper into the 2D perovskite. In general, 2D perovskites exhibit significantly enhanced moisture stability due to the organic cation spacers preventing diffusion of water molecules, however, we see that the lack of heavy elements in the spacer region contributing to the lower density of the 2D perovskite renders the film more vulnerable to acute irradiation. The e-beam irradiation damaged the PEA_2PbI_4 film (see Figure S8, Supporting Information) as indicated by the dark region around the grid and the grid itself exhibited negligible PL in comparison to an untreated region on the same film.

To further account for differences in the morphology between e-beam treated and untreated regions in 3D perovskites, surface profiles from the channel region in $MAPbI_3$ were measured using an atomic force microscope (AFM). As a consequence of the top layers of the film receiving large e-beam doses, the AFM data suggests that several monolayers have been removed during the process of e-beam treatment along with some morphological changes (see Figure S9, Supporting Information), although other explanations including densification are formally possible. In the case of e-beam treatment of the channel for photocurrent measurements as in Figure 4, 3.8 nm of the top surface of the film was apparently etched by the e-beam compared to the adjacent untreated region. In this manner, the material is sublimated off from the top surface until a layer further from the original surface receives a sufficiently low dose that is able to be withstood. At this dose, an effective annealing process occurs and the remaining surface experiences enhanced PL and conductive properties.

3. Conclusion

In conclusion, several hybrid perovskite thin film materials were grown using a multi-step CVD method and then exposed to e-beam irradiation at cryogenic temperatures. For the 3D perovskites, the PL was greatly enhanced. Differences in photoresponse properties were observed in $MAPbI_3$ and its defect passivated counterpart (during growth), $MAPbI_3$:Cl. Photocurrent measurements were conducted on samples with regions of e-beam irradiated channels wherein the photocurrent was significantly enhanced in the $MAPbI_3$ thin film likely due to a reduction in the defect density of the surface. Dynamic photocurrent measurements reveal the nature of trapping sites with a faster response time for e-beam treated $MAPbI_3$ whereas improvements to the photocurrent of the chlorine incorporated $MAPbI_3$:Cl films were minimal due to the passivation of defect sites by Cl ions during growth. The 2D perovskite, PEA_2PbI_4, was severely damaged by the e-beam even at very low dosage. The low mass density in the 2D perovskites confers a reduced resiliency towards e-beam irradiation, as seen in the Monte Carlo simulations. The e-beam penetration depth is almost 40% higher in PEA_2PbI_4 compared with $MAPbI_3$. Cryogenic e-beam patterning along with the CVD growth of 3D halide perovskites is a promising approach for enhancing the optoelectronic properties.

4. Experimental Section

Materials: Phenethylammonium iodide (PEAI), methylammonium iodide (MAI), lead (II) iodide (PbI_2 99%), and lead (II) chloride ($PbCl_2$ 98%) were purchased from Sigma-Aldrich (St. Louis, MO, USA) and were utilized without any purification or modifications.

CVD Growth: Vapor deposition processes were carried out using a two-zone furnace from SAFTherm (Model # STG-100-12-2). The furnace allowed for the independent control of the temperature between each zone with the interface region between zones I and II being highly insulated with different temperature control units. High purity (99.999%) nitrogen gas was used as a carrier in the reactor. The flow rate of the carrier gas was mediated via a mass flow controller from MTI Corporation. All growths were done in a multiple-step process. For the non-chlorine incorporated films, lead iodide was first sublimated at a 400 °C source temperature and carried downstream to a SiO_2 substrate held at 160 °C. The resulting compact lead iodide thin film was then exposed to organic iodide vapors (MAI, PEAI) and converted from lead iodide to the final perovskite in the second step. After the furnace heating curve concluded, the samples were slowly cooled in the reactor by maintaining the N_2 carrier gas flow for an hour at which point the furnace was opened and cooled by a fan. After another hour at this step, the inside of the reactor would be near room temperature, the nitrogen gas flow and vacuum pump would be turned off, and the reactor would then be exposed to atmospheric pressure wherein the samples were finally extracted. The chlorine incorporated $MAPbI_3$:Cl film was grown in a three step process as discussed in ref. [17]. The thickness of the 3D $MAPbI_3$ films was approximately 350 nm and that of PEA_2PbI_4 was approximately 250 nm.

50 nm thick gold contacts were deposited in a high vacuum deposition chamber (10^{-5} mbar) on top of the fully converted perovskite thin films. The gold formed a pattern where the channel width was 1000 µm and the channel length was 20–50 µm depending on the individual device. After the gold was deposited, perovskite films were then exposed to electron beam radiation in the channel region in a geometry ≈300 µm wide and with a length spanning the entire distance of each individual channel.

E-Beam Treatment: Samples were irradiated using a field emission scanning electron microscope (JSM-7001F, JEOL Inc.). The instrument is equipped with a cryogenic stage, a nanopattern generation system (JC Nabity Lithography Systems) and other custom features described previously.[60] Electron treatment for the exposure sweep tiles was performed at a temperature of 112 ± 4 K, at an acceleration voltage of 5 kV with a probe current of 0.9 ± 0.14 nA, which was incident on the sample with 1.987×10^8 e nm^{-2} s^{-1}. For the channel treatment, a pattern of 150 mm × 400 mm was exposed within a set of 100 µm wide channels at a temperature of 112 ± 4 K with the beam parameters set to 5 kV and probe current of 3.47 ± 0.14 nA (7.66×10^8 e nm^{-2} s^{-1}).

Characterization: X-Ray Diffraction: Grazing incidence temperature-dependent X-ray diffraction measurements were performed at sector 33-BM-C in the Advanced Photon Source at Argonne National Laboratory. The incidence angle was 2.9° and the temperature varied between 20 and 300 K.

Scanning Electron Microscope (SEM): During the e-beam treatment, the temperature sweep images were taken at 5 kV with a probe current of 13 pA. The SEM images were acquired at an acceleration voltage of 2–5 keV with a beam current of 50 pA. Other SEM images were acquired using a Thermo Scientific Apreo.

Photoluminescence (PL): The PL measurements were conducted in back-reflection geometry using a Renishaw inVia spectrometer. A 514 nm Ar^+ ion laser with a diameter spot size of <3 µm was used to excite the samples. The setup allowed for the visualization of the treated regions containing patterns with as small as 2×2 µm features where the laser could then be focused on individual tiles and regions on the sample.

Photocurrent and Dynamic Photocurrent: For the photocurrent measurements, a 532 nm laser diode was used as the excitation source in tandem with a Keithley 2400 source meter and a mechanical chopper for dynamic photocurrent measurements. For the steady state photocurrent measurements, the channel voltage was swept from −10 to +10 V while varying the laser power. The dynamic photocurrent measurements were measured with a lock-in amplifier (Zurich Instruments-MFLI). The chopper was set to a frequency of 2 Hz.

Atomic Force Microscope (AFM): Images were acquired in air using tapping mode on a commercially instrument (Asylum Research, Cypher) using OPUS Micro Cantilevers from µmasch (160AC-NA) with a nominal drive frequency of 300 kHz. The 256 × 256 pixel scans were carried at a speed of 12.52 µm s^{-1}.

Supporting Information

Supporting Information is available from the Wiley Online Library or from the author.

Acknowledgements

The authors acknowledge support of this work through the U.S. National Science Foundation (NSF) under Grant No. CMMI-2314347. The authors thank Evguenia Karapetrova from Argonne National Laboratory for measuring the temperature-dependent XRD and David Stalla from the University of Missouri for obtaining the SEM images. Use of the Advanced Photon Source was supported by the U.S. Department of Energy, Office of Science, Office of Basic Energy Sciences, under Contract No. DE-AC02-06CH11357.

Conflict of Interest

The authors declare no conflict of interest.

Author Contributions

R.B. synthesized the CVD grown perovskite films, conducted optical and photocurrent measurements, and analyzed the data. S.G. helped with some of the data analysis. C.J.A. helped with setting up of the CVD system. S.G. and G.K. conceived the work. D.C. and G.M.K. conducted the e-beam patterning of the perovskite films under cryogenic condition and AFM characterization. H.D. performed the Monte Carlo simulations. The manuscript was written by S.G. and R.B. with contributions from all authors. All authors have given approval to the final version of the manuscript.

Data Availability Statement

The data that support the findings of this study are available from the corresponding author upon reasonable request.

Keywords

chemical vapor deposition, electron beam irradiation, halide perovskite, photocurrent, photoluminescence, scanning electron microscope

Received: August 7, 2024
Revised: October 8, 2024
Published online: November 13, 2024

[1] NREL, https://www.nrel.gov/pv/cell-efficiency.html (accessed: July 2024).
[2] C. He, X. Liu, *Light Sci. Appl.* **2023**, *12*, 15.

[3] X. Yu, T. Shen, C. Zhu, Q. Zeng, A. Yu, S. Liu, R. Yi, Z. Weng, Y. Zhan, X. Hou, J. Qin, *ACS Appl. Nano Mater.* **2020**, *3*, 11889.
[4] J. Sun, J. Wu, X. Tong, F. Lin, Y. Wang, Z. M. Wang, *Adv. Sci.* **2018**, *5*, 1700780.
[5] L. Schmidt-Mende, V. Dyakonov, S. Olthof, F. Ünlü, K. M. T. Lê, S. Mathur, A. D. Karabanov, D. C. Lupascu, L. M. Herz, A. Hinderhofer, F. Schreiber, A. Chernikov, D. A. Egger, O. Shargaieva, C. Cocchi, E. Unger, M. Saliba, M. M. Byranvand, M. Kroll, F. Nehm, K. Leo, A. Redinger, J. Höcker, T. Kirchartz, J. Warby, E. Gutierrez-Partida, D. Neher, M. Stolterfoht, U. Würfel, M. Unmüssig, et al., *APL Mater.* **2021**, *9*, 109202.
[6] J. S. Manser, J. A. Christians, P. V. Kamat, *Chem. Rev.* **2016**, *116*, 12956.
[7] J.-C. Blancon, J. Even, C. C. Stoumpos, M. G. Kanatzidis, A. D. Mohite, *Nat. Nanotechnol.* **2020**, *15*, 969.
[8] Z. Zhu, V. G. Hadjiev, Y. Rong, R. Guo, B. Cao, Z. Tang, F. Qin, Y. Li, Y. Wang, F. Hao, S. Venkatesan, W. Li, S. Baldelli, A. M. Guloy, H. Fang, Y. Hu, Y. Yao, Z. Wang, J. Bao, *Chem. Mater.* **2016**, *28*, 7385.
[9] A. M. A. Leguy, Y. Hu, M. Campoy-Quiles, M. I. Alonso, O. J. Weber, P. Azarhoosh, M. van Schilfgaarde, M. T. Weller, T. Bein, J. Nelson, P. Docampo, P. R. F. Barnes, *Chem. Mater.* **2015**, *27*, 3397.
[10] B. P. Kore, M. Jamshidi, J. M. Gardner, *Mater. Adv.* **2024**, *5*, 2200.
[11] X. Yu, Y. Qin, Q. Peng, *J. Phys. Chem. A* **2017**, *121*, 1169.
[12] A. D. Taylor, Q. Sun, K. P. Goetz, Q. An, T. Schramm, Y. Hofstetter, M. Litterst, F. Paulus, Y. Vaynzof, *Nat. Commun.* **2021**, *12*, 1878.
[13] T. Zhang, F. Wang, H. Chen, L. Ji, Y. Wang, C. Li, M. B. Raschke, S. Li, *ACS Energy Lett.* **2020**, *5*, 1619.
[14] S. Ngqoloda, C. J. Arendse, T. F. Muller, P. F. Miceli, S. Guha, L. Mostert, C. J. Oliphant, *ACS Appl. Energy Mater.* **2020**, *3*, 2350.
[15] L. Fan, Y. Ding, J. Luo, B. Shi, X. Yao, C. Wei, D. Zhang, G. Wang, Y. Sheng, Y. Chen, A. Hagfeldt, Y. Zhao, X. Zhang, *J. Mater. Chem. A* **2017**, *5*, 7423.
[16] Y. Zhao, F. Ma, Z. Qu, S. Yu, T. Shen, H.-X. Deng, X. Chu, X. Peng, Y. Yuan, X. Zhang, J. You, *Science* **2022**, *377*, 531.
[17] R. Burns, S. Ngqoloda, S. C. Klue, E. Karapetrova, C. J. Arendse, S. Guha, *ACS Appl. Electron. Mater.* **2022**, *4*, 4258.
[18] J. Ran, O. Dyck, X. Wang, B. Yang, D. B. Geohegan, K. Xiao, *Adv. Energy Mater.* **2020**, *10*, 1903191.
[19] M. U. Rothmann, J. S. Kim, J. Borchert, K. B. Lohmann, C. M. O'Leary, A. A. Sheader, L. Clark, H. J. Snaith, M. B. Johnston, P. D. Nellist, L. M. Herz, *Science* **2020**, *370*, eabb5940.
[20] Y. Li, W. Zhou, Y. Li, W. Huang, Z. Zhang, G. Chen, H. Wang, G.-H. Wu, N. Rolston, R. Vila, W. Chiu, Y. Cui, *Joule* **2019**, *3*, 2854.
[21] Y. Zhu, Z. Gui, Q. Wang, F. Meng, S. Feng, B. Han, P. Wang, L. Huang, H.-L. Wang, M. Gu, *Nano Energy* **2020**, *73*, 104820.
[22] B. Jin, F. Liang, D. Zhao, Y. Lu, L. Liu, F. Liu, Z. Chen, G. Bi, P. Wang, Q. Zhang, M. Qiu, *Nano Lett.* **2022**, *22*, 7449.
[23] B. Jin, Y. Hong, Z. Li, D. Zhao, Y. Lu, G. Yao, R. Zheng, G. Bi, Q. Zhang, X. Fang, M. Qiu, *Nano Energy* **2022**, *102*, 107692.
[24] C.-W. Chen, H.-W. Kang, S.-Y. Hsiao, P.-F. Yang, K.-M. Chiang, H.-W. Lin, *Adv. Mater.* **2014**, *26*, 6647.
[25] J. Qiu, L. L. McDowell, Z. Shi, *Cryst. Growth Des.* **2019**, *19*, 2001.
[26] M. T. Hoerantner, E. L. Wassweiler, H. Zhang, A. Panda, M. Nasilowski, A. Osherov, R. Swartwout, A. E. Driscoll, N. S. Moody, M. G. Bawendi, K. F. Jensen, V. Bulović, *ACS Appl. Mater. Interfaces* **2019**, *11*, 32928.
[27] M. M. Tavakoli, L. Gu, Y. Gao, C. Reckmeier, J. He, A. L. Rogach, Y. Yao, Z. Fan, *Sci. Rep.* **2015**, *5*, 14083.
[28] A. Ham, T. S. Kim, M. Kang, H. Cho, K. Kang, *iScience* **2021**, *24*, 103486.
[29] C. J. Arendse, R. Burns, D. Beckwitt, D. Babaian, S. Klue, D. Stalla, E. Karapetrova, P. F. Miceli, S. Guha, *ACS Appl. Mater. Interfaces* **2023**, *15*, 59055.
[30] R. Burns, S. Ngqoloda, C. J. Arendse, B. Lavina, A. Dahal, D. K. Singh, S. Guha, *J. Mater. Res.* **2021**, *36*, 1805.
[31] F. Brivio, J. M. Frost, J. M. Skelton, A. J. Jackson, O. J. Weber, M. T. Weller, A. R. Goñi, A. M. A. Leguy, P. R. F. Barnes, A. Walsh, *Phys. Rev. B* **2015**, *92*, 144308.
[32] T. Baikie, Y. Fang, J. M. Kadro, M. Schreyer, F. Wei, S. G. Mhaisalkar, M. Graetzel, T. J. White, *J. Mater. Chem. A* **2013**, *1*, 5628.
[33] P. S. Whitfield, N. Herron, W. E. Guise, K. Page, Y. Q. Cheng, I. Milas, M. K. Crawford, *Sci. Rep.* **2016**, *6*, 35685.
[34] A. Bonadio, C. A. Escanhoela, F. P. Sabino, G. Sombrio, V. G. de Paula, F. F. Ferreira, A. Janotti, G. M. Dalpian, J. A. Souza, *J. Mater. Chem.* **2021**, *A9*, 1089.
[35] D. Zhao, A. Han, M. Qiu, *Sci. Bull.* **2019**, *64*, 865.
[36] Y. Hong, D. Zhao, J. Wang, J. Lu, G. Yao, D. Liu, H. Luo, Q. Li, M. Qiu, *Nano Lett.* **2020**, *20*, 8841.
[37] R. Zheng, D. Zhao, Y. Lu, S. Wu, G. Yao, D. Liu, M. Qiu, *Adv. Funct. Mater.* **2022**, *32*, 2112894.
[38] G. M. King, G. Schürmann, D. Branton, J. A. Golovchenko, *Nano Lett.* **2005**, *5*, 1157.
[39] S. Singh, C. Li, F. Panzer, K. L. Narasimhan, A. Graeser, T. P. Gujar, A. Köhler, M. Thelakkat, S. Huettner, D. Kabra, *J. Phys. Chem. Lett.* **2016**, *7*, 3014.
[40] J. K. Larsen, S.-Y. Li, J. J. S. Scragg, Y. Ren, C. Hägglund, M. D. Heinemann, S. Kretzschmar, T. Unold, C. Platzer-Björkman, *J. Appl. Phys.* **2015**, *118*, 035307.
[41] M. H. Wolter, B. Bissig, P. Reinhard, S. Buecheler, P. Jackson, S. Siebentritt, *Phys. Status Solidi C* **2017**, *14*, 1600189.
[42] H. Yuan, E. Debroye, K. Janssen, H. Naiki, C. Steuwe, G. Lu, M. Moris, E. Orgiu, H. Uji-i, F. De Schryver, P. Samorì, J. Hofkens, M. Roeffaers, *J. Phys. Chem. Lett.* **2016**, *7*, 561.
[43] S. J. Yoon, S. Draguta, J. S. Manser, O. Sharia, W. F. Schneider, M. Kuno, P. V. Kamat, *ACS Energy Lett.* **2016**, *1*, 290.
[44] M. C. Brennan, S. Draguta, P. V. Kamat, M. Kuno, *ACS Energy Lett.* **2018**, *3*, 204.
[45] S. Ngqoloda, C. J. Arendse, S. Guha, T. F. Muller, S. C. Klue, S. S. Magubane, C. J. Oliphant, *Sol. Energy* **2021**, *215*, 179.
[46] H. Lee, P. Boonmongkolras, S. Jun, D. Kim, Y. Park, J. Koh, Y.-H. Cho, B. Shin, J. Y. Park, *ACS Appl. Energy Mater.* **2023**, *6*, 1565.
[47] X. Tang, M. van den Berg, E. Gu, A. Horneber, G. J. Matt, A. Osvet, A. J. Meixner, D. Zhang, C. J. Brabec, *Nano Lett.* **2018**, *18*, 2172.
[48] B. Jin, D. Zhao, F. Liang, L. Liu, D. Liu, P. Wang, M. Qiu, *Research* **2021**, *2021*, 1.
[49] J. M. Azpiroz, E. Mosconi, J. Bisquert, F. De Angelis, *Energy Environ. Sci.* **2015**, *8*, 2118.
[50] C. Li, A. Guerrero, Y. Zhong, A. Gräser, C. A. M. Luna, J. Köhler, J. Bisquert, R. Hildner, S. Huettner, *Small* **2017**, *13*, 1701711.
[51] Y. Yuan, J. Huang, *Acc. Chem. Res.* **2016**, *49*, 286.
[52] J. A. Anta, G. Oskam, P. Pistor, *J. Chem. Phys.* **2024**, *160*, 150901.
[53] S. A. L. Weber, I. M. Hermes, S.-H. Turren-Cruz, C. Gort, V. W. Bergmann, L. Gilson, A. Hagfeldt, M. Graetzel, W. Tress, R. Berger, *Energy Environ. Sci.* **2018**, *11*, 2404.
[54] M. C. Schmidt, E. Gutierrez-Partida, M. Stolterfoht, B. Ehrler, *PRX Energy* **2023**, *2*, 043011.
[55] A. Jaffe, Y. Lin, C. M. Beavers, J. Voss, W. L. Mao, H. I. Karunadasa, *ACS Cent. Sci.* **2016**, *2*, 201.
[56] H. Demers, N. Poirier-Demers, A. R. Couture, D. Joly, M. Guilmain, N. de Jonge, D. Drouin, *Scanning* **2011**, *33*, 135.
[57] D. Drouin, A. R. Couture, D. Joly, X. Tastet, V. Aimez, R. Gauvin, *Scanning* **2007**, *29*, 92.
[58] R. Browning, T. Z. Li, B. Chui, J. Ye, R. F. W. Pease, Z. Czyzewski, D. C. Joy, *Scanning* **1995**, *17*, 250.
[59] D. C. Joy, S. Luo, *Scanning* **1989**, *11*, 176.
[60] A. Han, J. Chervinsky, D. Branton, J. A. Golovchenko, *Rev. Sci. Instrum.* **2011**, *82*, 065110.